A High-Efficiency Multimode Li–Ion Battery Charger With Variable Current Source and Controlling Previous-Stage Supply Voltage

Jiann-Jong Chen, Fong-Cheng Yang, Chien-Chih Lai, Yuh-Shyan Hwang, and Ren-Guey Lee, *Member, IEEE*

Abstract—A high-efficiency multimode Li–Ion battery charger with variable current source and controlling previous-stage supply voltage is presented in this paper. Using variable current source can achieve the goal of constant-current mode to charge the battery and control previous-stage supply voltage which could increase the efficiency of the multimode battery charger. Moreover, the charging mode adopted in this charger is applied by two types of dual-mode strategy decided by the value of the equivalent series resistance of the Li–Ion battery. This technique will reduce the damage of Li–Ion battery. The Li–Ion battery charger is designed with 0.35-μm CMOS double-poly four-metal processes. The experimental results show that the charger works well and the theoretical analysis can be confirmed. The average power efficiency of the multimode Li–Ion battery charger can be up to 91.2% under the average power of 1.24 W, and the accuracy of the adaptive reference voltage is up to 97.3%. The chip area is only 1.32×0.95 mm^2.

Index Terms—Adaptive reference voltage, Li–Ion charger, variable current source.

I. INTRODUCTION

THE POWER management IC is necessary for standby power of portable devices, such as cellular phones and personal digital assistants. This development has resulted in the increased demand for Li–Ion batteries. Several Li–Ion battery chargers based on bipolar junction transistors and BiCMOS charger ICs have been developed [1]–[4], so we try to design a Li–Ion battery charger used with a standard CMOS process to satisfy the demand. There are many battery strategies which have been proposed, such as constant trickle current, constant-current charge strategy, and constant-current/constant-voltage charge dual-mode strategy [5]. For reducing the damage of the battery, we adopt the strategy of the constant trickle current. However, it takes too much time to charge the battery, also called "the overnight charger." In order to save charging time, the second strategy is proposed. Using a larger charging current, it corrects the disadvantage of the first strategy and saves charging time efficiently. If the battery voltage is reaching the predicting level, the charging process is off, and the charging
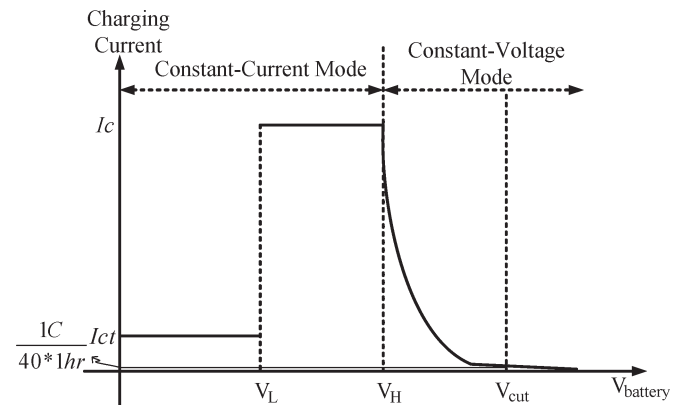
Fig. 1. Third strategy charging mode.

current is reduced to zero. However, the Li–Ion battery has different equivalent series resistance (ESR) in the whole charging process. If we offer excessive current to the battery with larger ESR, the battery could be overheated, so the damage of the battery can be probably made. For the reasons stated above, the constant-current/constant-voltage dual-mode strategy reduces the effectiveness of the drawbacks of other strategy. Fig. 1 shows the charge curve of the third strategy [6]. As shown in Fig. 1, if the battery voltage is less than V_L, the ESR of the Li–Ion battery is large. The trickle constant current is needed to charge battery. At this moment, the charger must be operated in constant-current mode. If the battery voltage is greater than V_L and less than V_H, the Li–Ion battery has small ESR. We can use larger constant current to charge it. In this situation, the charger is also operated in current mode. Eventually, if the battery voltage is greater than V_H, we use constant voltage to charge the battery and the charger is operated in voltage mode until the charging current is lower than $(1/40) * C/1$ h, (for 1 C $= 1000$ mA $\cdot$ h and 1 h $= 1$ h) [7]. It means that the Li–Ion battery can achieve full capacity and the entire process can also be completed. Generally speaking, the charging time of constant-voltage current is a short time, so the V_{cut} is very close to V_H.

There are many battery chargers which have been presented in [10]–[22]. When the battery charger is designed with switching-mode power supply (SMPS) converters, the passive elements are too huge to put them into the chip. Also, the battery chargers based on the switched-capacitor (SC) topology have the same problem, so the performance of power efficiency is not as good as expected [10]. There are some previous works
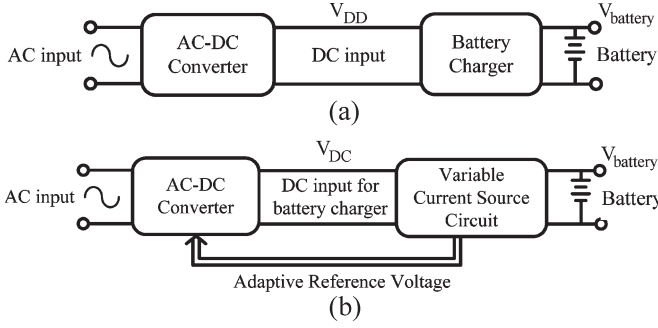
Fig. 2. (a) Traditional battery charger architecture. (b) Architecture of the proposed Li–Ion battery charger.

designed with the architecture of low-dropout (LDO) voltage regulator. Because the power source is a constant voltage in [1]–[4], and [6], the major problem of these chargers is low power efficiency in the initial process. Based on all of the aforementioned drawbacks, we proposed a method to implement a battery charger which uses variable current source and controls previous-stage supply voltage at the same time to increase the power efficiency in the battery charger stage. In this paper, the description of Li–Ion battery charger system will be included in Section II, and the stability analysis is shown in the Section III. The simulation and experimental results of charger are shown in Sections IV and V, respectively. Finally, the conclusions are made in Section VI.

II. CIRCUIT DESCRIPTIONS

A. Benefit of the Adaptive Reference Voltage

The general architecture of Li–Ion battery charger shown in Fig. 2(a) consists of the ac–dc converter and battery charger. In the traditional battery charger, the ac–dc converter is independent of the battery charger which is composed of the SMPS, SC or LDO topologies. Equation (1) shows the power efficiency of the traditional SC and LDO battery charger

$$\eta_1 \cong \frac{V_{\text{battery}} I_{\text{charge}}}{V_{\text{DD}}(I_q + I_{\text{charge}})} \cong \frac{V_{\text{battery}}}{V_{\text{DD}}}. \tag{1}$$

If the I_q is the quiescent current of the control circuit [8], it is usually much smaller than the charging current I_{charge}. Therefore, the efficiency is almost V_{battery} over V_{DD}. The V_{DD} is constant, so the η_1 is quite low in the initial process, and this is a serious shortcoming in the charger which uses SC or LDO topology. On the other hand, the variable current source circuit shown in Fig. 2(b) can produce an adaptive reference voltage, and it can control the output voltage of the ac–dc converter to keep the charger in high power efficiency for the whole time. Equation (2) shows the results of discussion above. When V_{battery} is changed, the V_{DC} follows the V_{battery} with a fixed voltage (our preset value is 0.3 V). The η_2 is shown in (2), and the efficiency is increasing by variable current source. Meanwhile, the proposed charger can also support constant-current, and constant-voltage operational modes to charge a Li–Ion battery

$$\eta_2 \cong \frac{V_{\text{battery}} I_{\text{charge}}}{V_{\text{DC}}(I_q + I_{\text{charge}})} \cong \frac{V_{\text{battery}}}{V_{\text{DC}}} = \frac{V_{\text{battery}}}{V_{\text{battery}} + 0.3}. \tag{2}$$
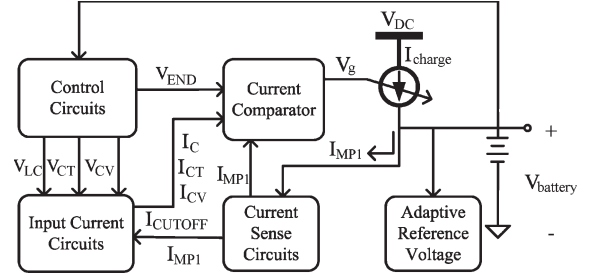

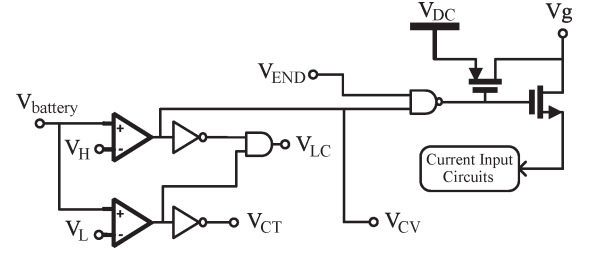Fig. 3. Architecture of the variable current source circuit.

Fig. 4. Charging control circuit.

TABLE I
CHARGING CONTROL CIRCUIT FUNCTION

Condition	V_{CT}	V_{LC}	V_{CV}	V_{END}	V_g
Constant trickle current	Hi	Lo	Lo	Lo	Lo
Constant large current	Lo	Hi	Lo	Lo	Lo
Constant Voltage current	Lo	Lo	Hi	Lo	Lo
I_{MP1} smaller than $(1/40)*C/1hr$	Lo	Lo	Hi	Hi	Lo
Process terminated	Lo	Lo	Hi	Hi	Hi

B. Architecture of the Variable Current Source

In Fig. 3, it shows the architecture of the multimode variable current source circuit that includes the control circuit, input current circuit, current comparator, current sense circuit, and adaptive reference voltage circuit. The V_{DC} is the output voltage of the previous ac–dc converter, and the V_g is used to control I_{charge} current to maintain constant charging current in the different charging modes.

C. Charging Control Circuit

Continuously, Fig. 4 shows the charging control circuit. When the battery voltage V_{battery} is less than V_L, the battery charger is operated in the constant-current mode with trickle charging current; when V_{battery} is greater than V_L and less than V_H, the battery charger is operated in the constant-current mode with higher charging current. When V_{battery} is greater than V_H, the battery charger is in the constant-voltage mode. If charging current reduces to $(1/40)*C/1$ h, the V_g will be high and turn off the Power MOSFET transistors. Then, the charging process is completed. As shown in Table I, the function of the charging control circuit is described.

D. Input Current Circuit

Fig. 5 shows the input current circuits. The OP1 and R_{REF} are used to produce the accurate reference current to charge
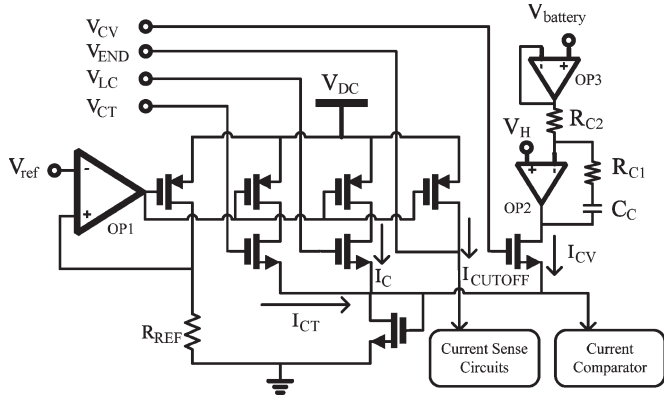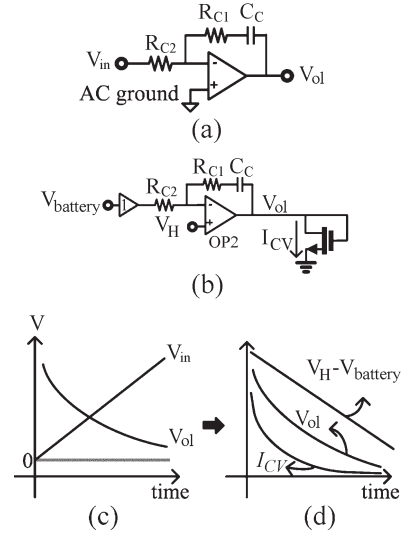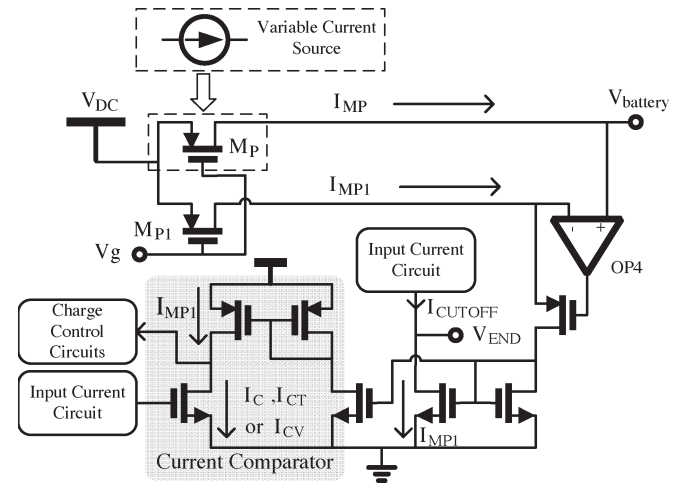
Fig. 5. Input current circuit.

Fig. 6. (a) Basic structure of the integrator. (b) I_{CV} generating circuits. (c) Time-domain diagram of the integrator. (d) Time-domain diagram when $V_{battery} > V_H$.

Li–Ion battery. The V_{CT}, V_{LC}, and V_{CV} are control signals from charging control circuits, and they can turn on or turn off the switches in the corresponding charging phase.

The current I_{CT}, I_C, and I_{CV} are three kinds of the charging current for the Li–Ion battery. The OP3 is used to isolate the battery voltage, and we employ OP2 to make the I_{CV} current, and (3)–(6) show how to generate I_{CV} current

$$V_{o1} = \Delta V_{battery} \left[-\frac{1+sC_C R_{C1}}{sC_C R_{C2}} \right]$$

$$\cong (V_H - V_{battery}) \left[-\frac{1+sC_C R_{C1}}{sC_C R_{C2}} \right] \quad (3)$$

$$I_{CV} = \beta_n (V_{o1} - V_{th})^2 \quad (4)$$

$$V_{o1} = \Delta V_{battery} \left[-\frac{1+sC_C R_{C1}}{sC_C R_{C2}} \right]$$

$$=> -\Delta V_{battery} \left[\frac{1}{C_C R_{C2}} u(t) + \frac{R_{C1}}{R_{C2}} \delta(t) \right]$$

$$\cong -\Delta V_{battery} \left(\frac{1}{C_C R_{C2}} u(t) \right) \cong -\frac{\Delta V_{battery}}{C_C R_{C2}} \bigg|_{t>0} \quad (5)$$

$$I_{CV} \cong \beta_n \left[(V_H - V_{battery}) \frac{1}{C_C R_{C2}} + V_{th} \right]^2$$

$$\cong \beta_n \left[\frac{\Delta V_{battery}}{C_C R_{C2}} + V_{th} \right]^2 \bigg|_{t>0}. \quad (6)$$

Fig. 6(a) shows the basic structure of the integrator, and Fig. 6(c) shows its time-domain diagram. Generally speaking, when V_{in} is getting larger than zero gradually, the V_{o1} is decreasing. Based on this phenomenon, we could utilize a simple $V-I$ converter for Fig. 6(a) to generate I_{CV} current shown in Fig. 6(d). Therefore, we could adopt an integrator and a simple $V-I$ MOS to generate I_{CV} current in Fig. 6(b). Continuously, Fig. 6(b) shows the I_{CV} generating circuit which is combined with an integrator. From Fig. 6(b), we could get (3) and (4), and we use the Inverse Laplace Transform to obtain (5). Next, we replace (5) into (4) to get (6). Hence, if the $\Delta V_{battery}$ is becoming a negative value (it means the $V_{battery}$ is larger than V_H), the I_{CV} is decreasing gradually. Moreover, the V_{END} is the output signal to be sent into the charging control circuit which is shown in Fig. 5. If the I_{MP1} is smaller than I_{CUTOFF} in Fig. 7, the M_P and M_{P1} will be shut down.

Fig. 7. Current sense circuit.

E. Current Sense Circuit

As shown in Fig. 7, we use the MOSFET transistor M_P to replace the variable current source. According to the different charging modes, the V_g adjusts the gate terminal of M_P to produce the exceptional charging current. Moreover, the M_{P1} is used in the current sense circuit to sense the current on power MOSFET M_P. We used the operational amplifier OP4 to make the source-to-drain voltages, V_{SD} of M_{P1} and M_P be equal. The currents of M_{P1} and M_P can be described as the following equations:

$$I_{MP1} = \frac{1}{2} \mu_n C_{ox} \frac{W_{P1}}{L_{P1}} \left[2(V_{SG} - |V_{thp}|) V_{SD} - V_{SD}^2 \right] \quad (7)$$

$$I_{MP} = \frac{1}{2} \mu_n C_{ox} \frac{W_P}{L_P} \left[2(V_{SG} - |V_{thp}|) V_{SD} - V_{SD}^2 \right] \quad (8)$$

where μ_P is the mobility of a PMOS transistor, C_{ox} is the gate capacitance per unit area, and V_{thp} is the threshold voltage of a PMOS transistor. In this way, the power MOS is operated in
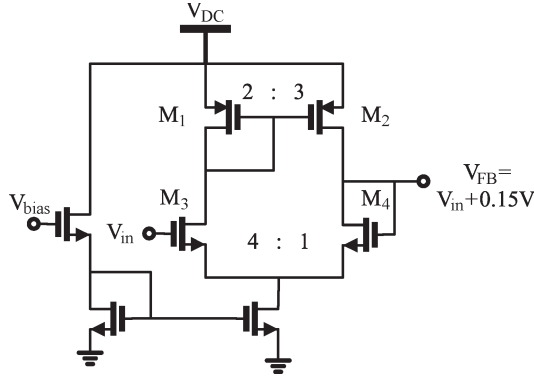
Fig. 8.   Level shift circuits.

the triode region to minimize the power dissipation on M_P. Since the negative feedback of the operational amplifier OP4 will force the source-to-drain voltages V_{SD} of M_{P1} and M_P to be equal, the I_{MP} and I_{MP1} are almost proportional to their aspect ratios. Their current ratio can be described as

$$\frac{I_{MP1}}{I_{MP}} \cong \frac{\left(\frac{W_{P1}}{L_{P1}}\right)}{\left(\frac{W_P}{L_P}\right)} = \frac{1}{N}. \tag{9}$$

In (9), the I_{MP1} and I_{MP} make a ratio, and I_{MP1} is reduced to 1/6000 of I_{MP}, proportionally. Another circuit is current comparator which compares the input current with I_{MP1}. Then, it produces a signal to control the gate of the power MOSFET, by this control loop, the output charging current would charge the battery in terms of our charging method, and for this reason, it can make sure the power MOS M_{P1} to be a variable current source, and we can use it to charge the battery in the different constant current phases.

F. Level Shift Circuit and Adaptive Reference Voltage

Shown in Fig. 8 is the level shift circuit. The level shift circuit is applied in the complete charger circuit, as shown in Fig. 9. We use the OP-based circuit to product a level shift voltage. Meanwhile, we change the aspect ratios of M_1, M_2, M_3, and M_4 to create an expected level shift (our preset value is 0.15 V). In Fig. 9, we used two diode-connected PMOS transistors and the level shift circuit to produce the adaptive reference voltage V_{FB}. Moreover, we combined every function blocks to construct the multimode variable current source circuit. Finally, the adaptive reference voltage can be the V_{FB} shown in (10). From the description above, we have already explained how the variable current source circuit charges the Li–Ion battery in the constant current phase.

After the constant current phase, the battery charger is operated in the constant voltage phase, and we make the output voltage of ac–dc converter V_{DC} to be the constant value and to follow the battery voltage [23]. Eventually, the battery charger can achieve the goals of constant voltage and high efficiency

$$V_{FB} = \frac{1}{2}(V_{battery} + 0.3). \tag{10}$$

G. Flyback AC–DC Converter With Adaptive Reference Voltage

From the above circuits, we describe the proposed multimode variable current source circuit in detail. Then, we briefly introduce the ac–dc converter and show how to control previous-stage supply voltage. For the variable current source, the ac–dc converter must fulfill several specifications.
1) The loop gain of a flyback converter that operates in discontinuous conduction mode (DCM) is a one-pole system, so we could easily compensate the whole system with our proposal.
2) The flyback converter that operates in DCM mode has a better power factor.
3) For our application, our charger has a lower loading current for flyback converter (it compares with several amperes), so it is easy to control under DCM mode.

For the reasons stated above, we use the flyback converter.

As shown in Fig. 10, it is the function block of the ac–dc converter in the gray block and consists of the bridge rectifier, flyback converter, error amplifier, compensator, and optical coupler. The chip ICE2A0565Z produced by Infineon Technologies is used as a flyback controller [9], and it contains a power MOSFET inside. The error amplifier and compensator are used to compare the half of V_{DC} and adaptive reference voltage V_{FB} in the meantime. It can control the output voltage of the ac–dc converter to achieve the function of the adaptive reference voltage for the variable current source circuit, and we can maintain the V_{SD} of the power MOS M_{P1} to be a constant value in the whole charging time for reducing power dissipation on M_{P1}. The purpose of the optical coupler is to isolate the noise and separates the input and output side. The advantage is that the signal is unidirectional, without loading effects. The functions of the blocks are introduced separately in the above figure. The components of the ac–dc converter are described later in this paper. The detail ac–dc converter is shown in Fig. 11. The ac input is 110 V (rms), and the bridge rectifier can convert ac input to a dc output with ripple. The dc value is about 155 V. The next one is the transformer, and it is used to transfer dc voltage from the primary side to secondary side, like V_{DC}, V_{CC_5V}, and V_{CC_15V}. The V_{DC} provides the controllable supply voltage to the battery charger for high power efficiency. Meanwhile, the V_{CC_5V} supplies constant voltage to the operational amplifier LM358, optical coupler PC817, and the other auxiliary components. The last one is V_{CC_15V} that affords the supply voltage to the flyback controller chip ICE2A0565Z. This chip has the function of current sensing, so it could operate in the boundary condition and detect overcurrent at the output terminal.

III. STABILITY ANALYSIS

In order to analyze the stability for the charger, we must establish the small-signal model of the variable current source circuit with adaptive reference voltage.

A. Frequency Response of Flyback Converter Operated in DCM Mode

In proposed circuit, we adopted the DCM flyback controller in the front-end ac–dc converter. In Fig. 12, the small-signal
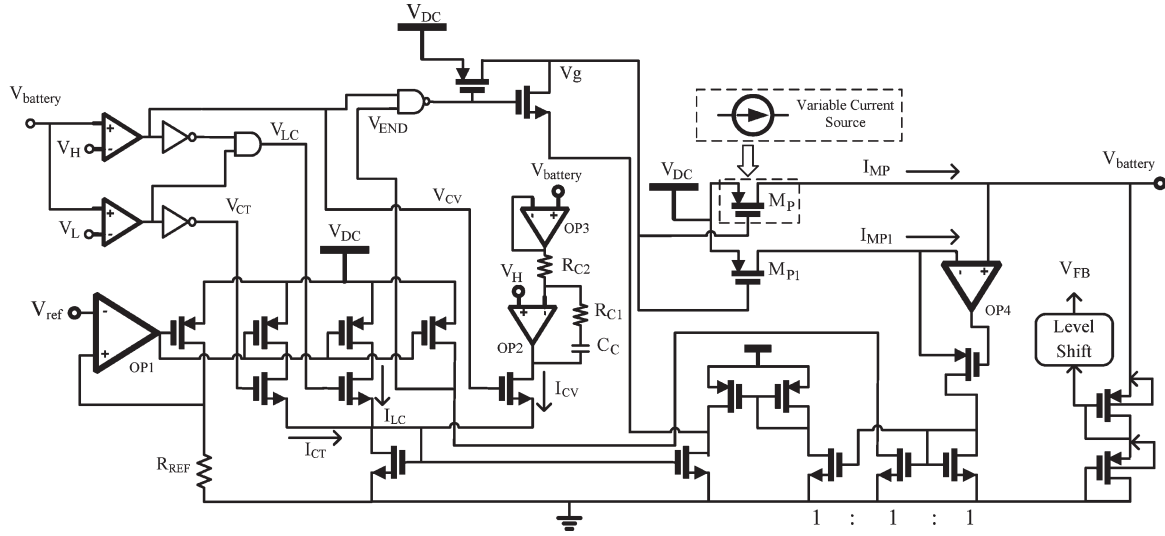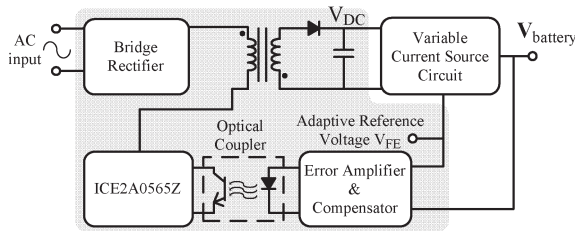
Fig. 9.   Complete charger circuit.

Fig. 10.   Architecture of the ac–dc converter.

model is shown for the entire battery charger. The transfer function $G_{vd}(s)$ is the transfer function of the flyback converter operated in DCM mode, and is shown as follows [13]:

$$G_{vd}(s) = K_{vd}\frac{\left(1-\frac{s}{\omega_{zRHP}}\right)\left(1+\frac{s}{\omega_{zc}}\right)}{\left(1+\frac{s}{\omega_{p1}}\right)\left(1+\frac{s}{\omega_{p2}}\right)} \quad (11)$$

where $K_{vd} = (V_{AC}/n\sqrt{k})$ and $k = (2Lf_s/R_L)$

$$\omega_{p1} = \frac{2}{R_L C} \quad (12)$$

$$\omega_{p2} = \frac{n^2 R_L}{L(M+1)^2} \quad (13)$$

$$\omega_{zRHP} = \frac{n^2 R_L}{LM(M+1)} \quad (14)$$

$$\omega_{zc} = \frac{1}{r_c C} \quad (15)$$

where $M = (V_{DC}/V_{AC}) = nD(1/\sqrt{k})$.

According to (11), there are two zeros and two poles in the transfer function, where V_{AC} is the rms value of the ac input voltage, n is the ratio of the transformer, L is the inductance of the transformer, C is the output capacitor of the flyback converter, f_s is the switching frequency, r_c is the ESR of the output capacitor, and R_L is the equivalent output impedance of the ac–dc converter. In (12) and (13), ω_{p2} and ω_{zRHP} are much greater than the other poles and zeros, so we can neglect them in the $G_{vd}(s)$. To simplify the analysis in the next step,

we neglect the ω_{zc} in the $G_{vd}(s)$. At last, (11) is simplified to (16) and shown in Fig. 12(a)

$$G_{vd}(s) \cong K_{vd}\frac{1}{\left(1+\frac{s}{\omega_{p1}}\right)}. \quad (16)$$

B. Frequency Response of Variable Current Source Circuit

Continuously, two parts are separated in this charging mode: one is the constant current mode and the other is constant voltage mode. In the constant current mode, we could calculate the inner open-loop gain as

$$\begin{aligned} inner\ &open\text{-}loop\ gain \\ &\cong \beta_1 G_{vc}(s)\frac{1}{V_M}G_{vd}(s) \\ &= \frac{1}{2}\frac{1+sC_{F1}R_{F1}}{sC_{F1}R_{F2}}\frac{1}{V_M}K_{vd}\frac{1}{\left(1+\frac{s}{\omega_{p1}}\right)} \\ &= K'_{vd}\frac{1+sC_{F1}R_{F1}}{sC_{F1}R_{F2}}\frac{1}{\left(1+\frac{s}{\omega_{p1}}\right)} \quad (17)\end{aligned}$$

where $K'_{vd} = (1/2)(1/V_M)K_{vd}$.

The voltage V_M is the coefficient of the pulsewidth modulation modulator in the flyback DCM controller, and we preset $\beta_1 = 1/2$. In Fig. 12(b), (18) shows the inner closed-loop gain $T_2(s)$

$$\begin{aligned} closed\text{-}loop\ gain = T_2(s) &\cong \frac{G_{vc}(s)\frac{1}{V_M}G_{vd}(s)}{1+\beta_1 G_{vc}(s)\frac{1}{V_M}G_{vd}(s)} \\ &= \frac{2K'_{vd}\frac{1}{\left(1+\frac{s}{\omega_{p1}}\right)}}{1+K'_{vd}\frac{1+sC_{F1}R_{F1}}{sC_{F1}R_{F2}}\frac{1}{\left(1+\frac{s}{\omega_{p1}}\right)}} \\ &= \frac{2sC_{F1}R_{F2}}{\left(1+\frac{s}{\omega'_{p1}}\right)\left(1+\frac{s}{\omega'_{p2}}\right)} \quad (18)\end{aligned}$$

where $\omega'_{p1} = (K'_{vd}/C_{F1}R_{F2})$ and $\omega'_{p2} = (2/R_L C)$.
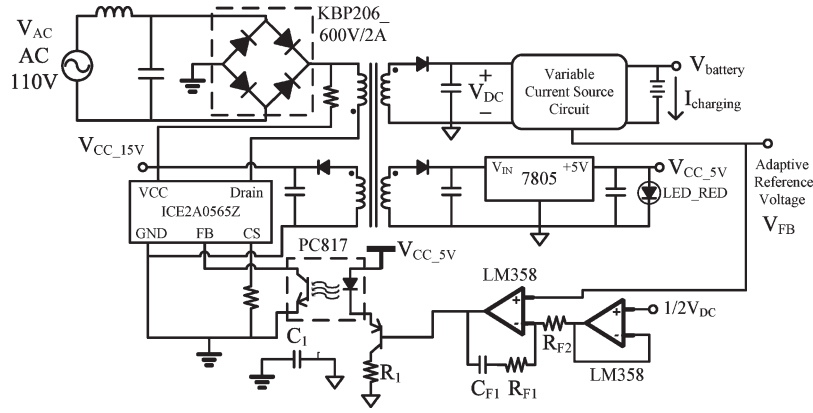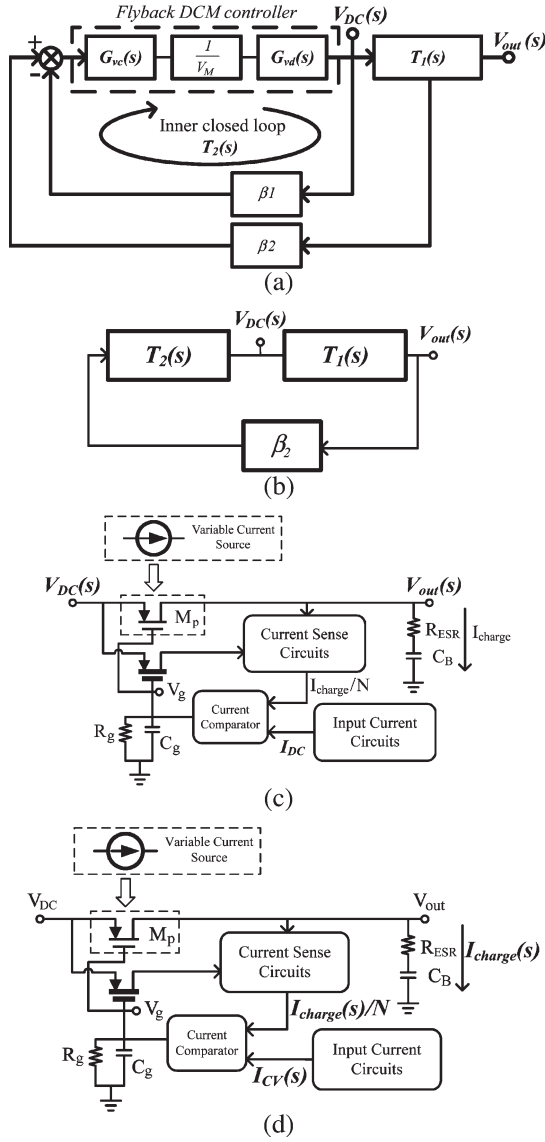
Fig. 11.   Complete ac–dc converter.

Fig. 12.   Small-signal model of the battery charger. (a) Signal flowchart of the entire charger. (b) Simplified signal flowchart of the entire charger. (c) Simple model of the constant-current mode. (d) Simple model of the constant-voltage mode.

In Fig. 12(c), the input current I_{DC} compares with feedback current I_{charge}/N, which is sensed from the charging current I_{charge}. The output voltage can control the gate of the

power MOSFET, V_g, to maintain the constant charging current. According to Fig. 12(c), (19) is accomplished. Finally, the transfer function $T_1(s)$ is concluded by (20)–(22) to confirm the theorem

$$V_{out}(s) = -g_{mp}\left[\left(R_g//\frac{1}{sC_g}\right)\frac{I_{charge}}{N} - V_{DC}(s)\right]\left(R_{esr}+\frac{1}{sC_B}\right) \tag{19}$$

where the g_{mp} is the transconductor of the Power MOSFET M_p

$$\begin{aligned} open\text{-}loop\ gain &\cong \beta_2 T_2(s) T_1(s)\\ &= \beta_2 \frac{2sC_{F1}R_{F2}}{\left(1+\frac{s}{\omega'_{p1}}\right)\left(1+\frac{s}{\omega'_{p2}}\right)}T_1(s)\\ &= \frac{1}{2}\frac{2sC_{F1}R_{F2}}{\left(1+\frac{s}{\omega'_{p1}}\right)\left(1+\frac{s}{\omega'_{p2}}\right)}\frac{V_{out}(s)}{V_{DC}(s)} \end{aligned} \tag{20}$$

$$I_{charge} = \frac{V_{out}}{\left(R_{esr}+\frac{1}{sC_B}\right)} \tag{21}$$

$$\begin{aligned} T_1(s) &= \frac{V_{out}(s)}{V_{DC}(s)}\\ &= \frac{g_{mp}(sC_B R_{esr}+1)}{sC_B\left(1+\frac{g_{mp}R_g}{N}+sC_g R_g\right)}. \end{aligned} \tag{22}$$

C. Frequency Response of Whole System

In the next step, we calculate the transfer function of the multimode Li–Ion battery charger and add the transfer function $T_2(s)$ of the flyback with DCM control to complete the total transfer function. Eventually, the entire transfer function with constant-current mode is shown in (23). Fig. 13 shows the frequency response for the constant current mode

$$\begin{aligned} loop\ gain\\ &\cong \frac{1}{2}\frac{2sC_{F1}R_{F2}}{\left(1+\frac{s}{\omega'_{p1}}\right)\left(1+\frac{s}{\omega'_{p2}}\right)}\frac{g_{mp}(sC_B R_{esr}+1)}{sC_B\left(1+\frac{g_{mp}R_g}{N}+sC_g R_g\right)}\\ &\cong g_{mp}R_{F2}\frac{1}{1+\frac{g_{mp}R_g}{N}}\frac{C_{F1}}{C_B}\frac{(sC_B R_{esr}+1)}{\left(1+\frac{s}{\omega'_{p1}}\right)\left(1+\frac{s}{\omega'_{p2}}\right)} \end{aligned} \tag{23}$$

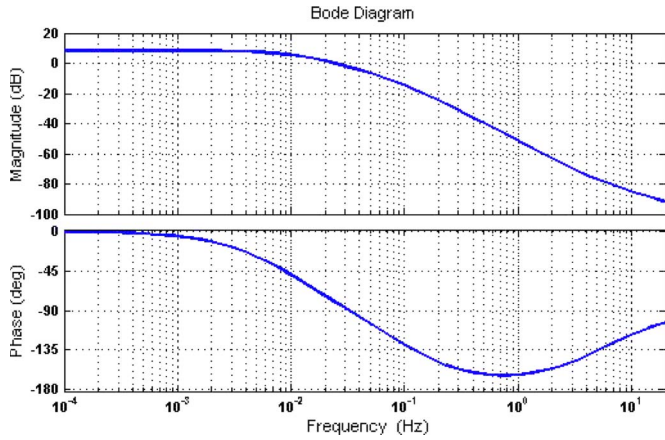where $\omega'_{p1} = (K'_{vd}/C_{F1}R_{F2})$ and $\omega'_{p2} = (2/R_L C)$.

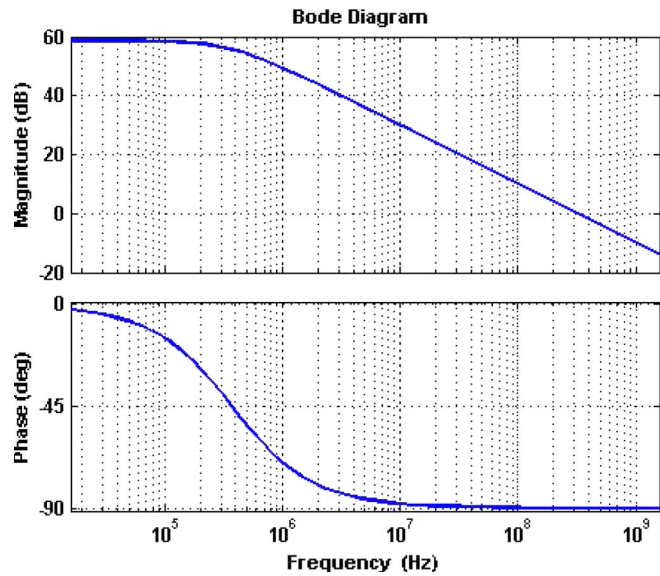Fig. 13. Frequency response for constant-current mode $V_{\text{out}} = 2.9$ V and $I_{\text{charge}} = 300$ mA.

Fig. 16. Simulation results of sensing currents, from top to bottom, the waveforms are the charging current I_{charge} and the sensed current I_{MP1}, respectively (horizontal scale: 50 s/div and vertical scale: 0.2 A/div and 50 μA/div, respectively, from top to bottom).

Fig. 14. Frequency response for constant-voltage mode.

Fig. 17. Simulation results of I_{CV} currents, from top to bottom, the waveforms are the charging current I_{charge} and the sensed current I_{MP1}, respectively (horizontal scale: 0.5 s/div and vertical scale: 0.2 A/div and 50 μA/div, respectively, from top to bottom).
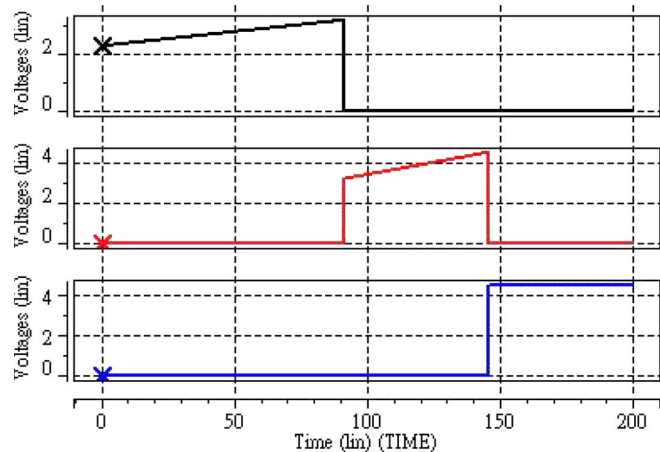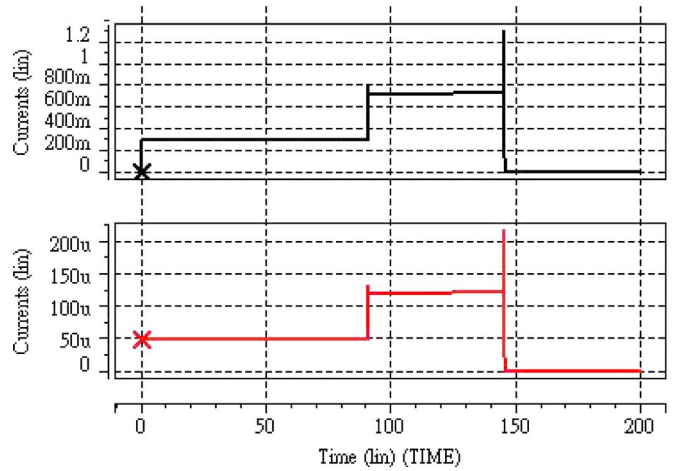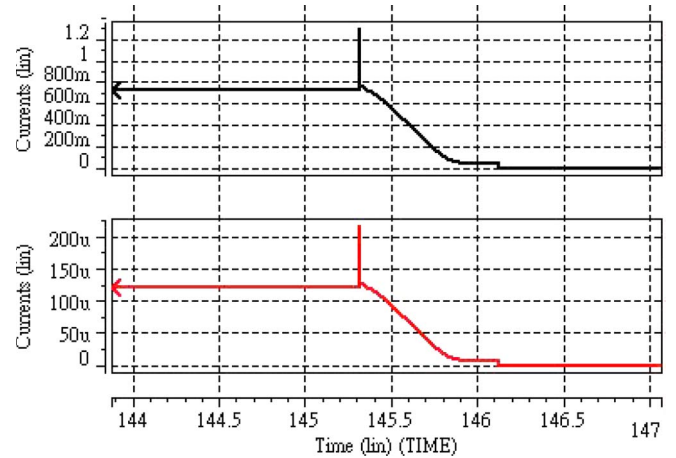

Fig. 15. Simulation results of the control signal in the charging control circuit, from top to bottom, the waveforms are the control signal V_{CT}, V_{LC}, and V_{CV}, respectively (horizontal scale: 50 s/div and vertical scale: 2 V/div, respectively).
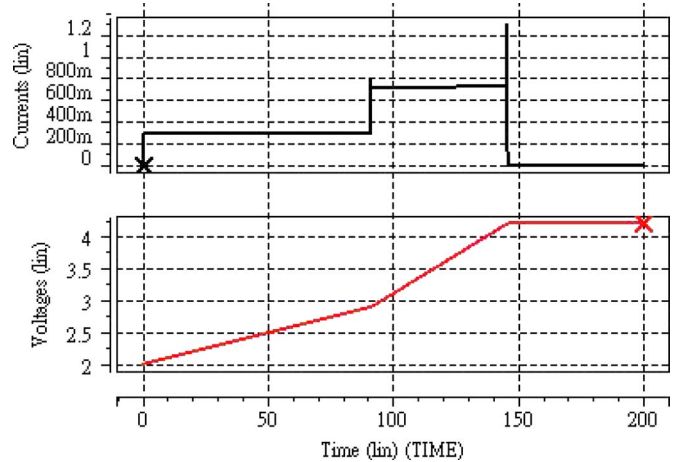

Fig. 18. Simulation results of output voltage and current, from top to bottom, the waveforms are the charging current I_{charge} and the battery voltage V_{battery}, respectively (horizontal scale: 50 s/div and vertical scale: 0.2 A/div and 0.5 V/div, respectively, from top to bottom).
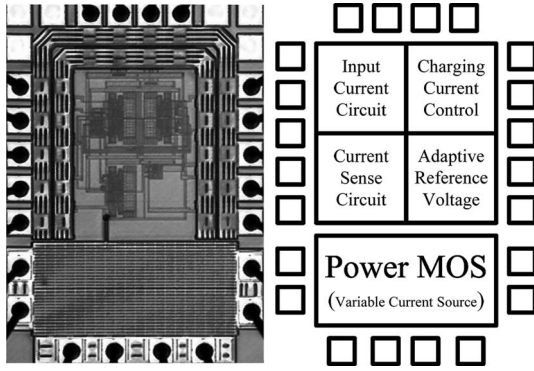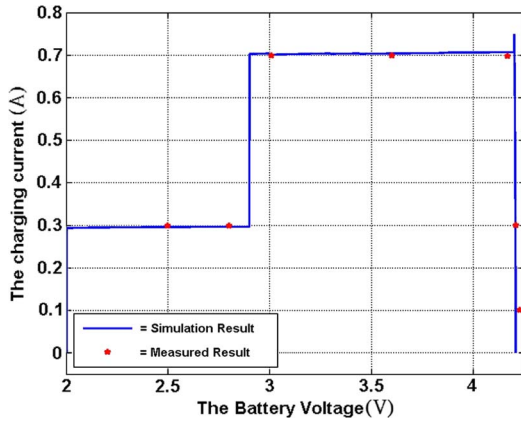
Fig. 19.   Photograph of proposed charger.

Fig. 20.   Simulation result and measured results. The blue line is simulation result, and the red star is measured results (horizontal scale: 0.5 V/div and vertical scale: 0.1 A/div, respectively, from top to bottom).
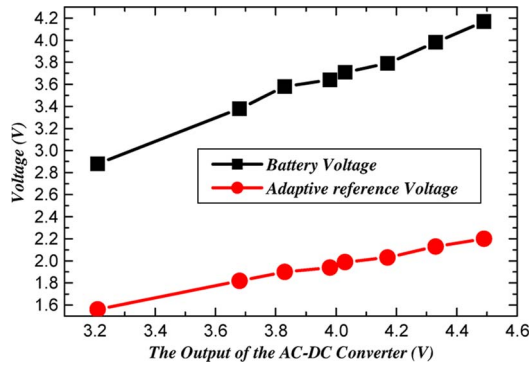

Fig. 21.   Curves of the battery and adaptive reference voltage for the output of the ac–dc converter.

In the constant-voltage charging mode, because the voltage of the system is stable in the constant voltage mode, shown in Fig. 12(d), we consider the variation of the charging current only. The result is shown in (24). In (24), there is a single pole in the transfer function, so it is an unconditionally stable system. Meanwhile, Fig. 14 shows the frequency response for the constant-voltage mode

$$I_{\text{charge}}(s) = - g_{\text{mp}} \left(R_{\text{g}} // \frac{1}{sC_{\text{g}}} \right) \left[\frac{I_{\text{charge}}}{N} - I_{\text{CV}}(s) \right] \Rightarrow$$

$$\frac{I_{\text{charge}}(s)}{I_{\text{CV}}(s)} = \frac{g_{\text{mp}} R_{\text{g}} N}{N + g_{\text{mp}} R_{\text{g}}} \frac{1}{1 + sC_{\text{g}} \frac{R_{\text{g}}}{\left(1 + \frac{g_{\text{mp}} R_{\text{g}}}{N} \right)}}. \quad (24)$$
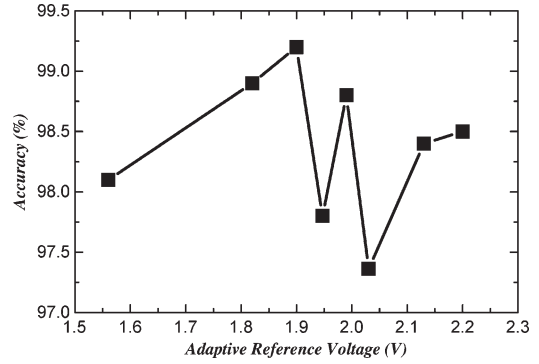

Fig. 22.   Curve of the accuracy for adaptive reference voltage.

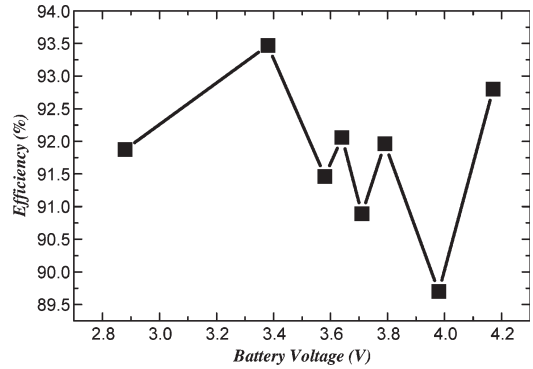
Fig. 23.   Curve of the efficiency for entire system.

TABLE II
SPECIFICATIONS OF THE PROPOSED CHARGER

Technology	TSMC 0.35μm 2P4M
Power supply voltage	2.3-4.5V
Average power consumption	1.24W
Average power efficiency	91.2%
Output voltage	2.0V-4.2V
Maximum switching frequency	100k Hz
Maximum charging current	698mA
V_H voltage	4.2 V
V_L voltage	2.9 V
Chip area (including PAD)	1.32 mm x 0.95 mm

In the whole charging time, the constant-current phase usually takes many time to charge battery (it usually spends several minutes.), so the unit-gain frequency in CC phase is not needed to be wide. In fact, the stability in battery charger is more important than the bandwidth. If the phase margin is not good enough, it is possible to fail to control over the V_{DC} (the supply voltage of the variable current source circuit). Therefore, the system in constant current mode is stable and shown in Fig. 13. Continuously, in the constant-voltage mode, we use the I_{CV} generating circuit to produce the I_{CV} and send it into the charger to charge the battery, so the charging current could be decreasing gradually. Moreover, we use the digital way to switch the CC and CV mode. When the CC mode changes to CV mode, it must be very fast. Otherwise, it maybe produces

TABLE III
COMPARISON SHEET

Parameter	2007 [10]	2007[11]	2005 [16]	2006 [17]	This work
Technology	TSMC 0.35μm 2P4M	NA	NA	AMI 0.5μm technology	TSMC 0.35μm 2P4M
Power supply voltage	5V	24V	3.9V	2.7-4.5V	2.3-4.5V
Average power consumption	837mW	NA	NA	NA	1.24W
Output voltage	4.2V	10V	2.5-4.2V	2.5V-4.2V	2.0V-4.2V
Maximum switching frequency	10MHz	18kHz	20kHz	600kHz	100kHz
Maximum charging current	694mA	2A	1A	800 mA	698mA
Chip area (with PADs)	1.455mm x 1.348mm	NA	NA	NA	1.32 mm x 0.95 mm
Average power efficiency	**67.89%**	**84%**	**55%**	**85 %**	**91.2%**

the spike current to damage battery between CC and CV mode. Consequently, the response of the CV mode must be quite fast, and Fig. 14 confirms this theory.

IV. SIMULATION RESULTS

The simulation results of the proposed charger using HSpice are shown in Figs. 15–18. The signals of control circuit are shown in Fig. 15, and the supply voltage varies by the voltage level of the battery. The simulation results of sensing current and measured current in the current sensing circuit are confirmed with theoretical analysis, shown in Fig. 16. In Fig. 17, it shows the I_{CV} current from Fig. 16. As shown in Fig. 18, the waveform is the battery voltage variation during charging interval. In the initial condition, it is supposed that the battery is in the low capacity (the preset value is 2.7 V). The power supply of the charger is 3 V, and the battery voltage changed from 2.7 to 4.2 V. The maximum output current is 710 mA, as the output voltage of the battery is over 2.9 V and under 4.2 V. The current always keep constant, and that is very suitable current for charging into Li–Ion batteries as the battery voltage under 4.2 V. On the other hand, there are three kinds of currents during charging interval in Fig. 18. The first phase shows the small current due to large internal resistance of battery. The second phase shows the large current due to the small internal resistance of battery. The first and second phases are both constant-current modes for the purpose of rapid charging. The third phase is constant-voltage mode operation to prevent the battery from damages. In this phase, the battery is almost full. The average power efficiency can achieve 91.2%.

V. EXPERIMENTAL RESULTS

To verify the circuit performance of the charger, the proposed converter is designed and implemented with 0.35-μm CMOS double-poly four-metal processes. The photograph of the proposed converter is shown in Fig. 19. The experimental results of the proposed charger which can support the output current I_{charge} as the charging current are shown in Fig. 20. We plot some measured points versus simulation result in Fig. 20.

Fig. 21 shows the curves of the battery and adaptive reference voltage for the output of the ac–dc converter. Fig. 22 shows the adaptive reference voltage versus accuracy. It means the adaptive reference voltage is more accurate, the battery voltage is located in our desired level. If the adaptive reference voltage is not accurate, the battery maybe is not totally charged or

overcharged. Fig. 23 shows the efficiency of the entire system. In particular, when the accuracy of the adaptive reference voltage is better, the power efficiency is much higher. Finally, we summarize the measured specifications of the proposed Li–Ion battery charger in Table II. Then, we compare the performance of the proposed charger with other battery chargers and list the comparison table in Table III. The power efficiency of the proposed charger is 91.2%, and it is greater than the others.

VI. CONCLUSION

In this paper, a high-efficiency charger using the variable current source and controlling previous-stage supply voltage has been developed by implementing 0.35-μm CMOS double-poly four-metal processes. From Fig. 23, we can understand an important phenomenon: that the greater accuracy of the adaptive reference voltage can make the higher efficiency of the entire system. The main advantages of this scheme is threefold.

1) We realize a multimode Li–Ion battery charger to charge a Li–Ion battery efficiently by controlling previous-stage supply voltage.
2) This paper results show this proposed charger operated in constant-current/constant-voltage dual mode can have higher power efficiency and its average efficiency is 91.2%.
3) The adaptive reference voltage is more accurate, the battery voltage is located in our desired level, precisely. If the adaptive reference voltage is not accurate, the battery maybe is not totally charged or overcharged.

REFERENCES

[1] S.-H. Jung, Y.-J. Woo, N.-I. Kim, and G.-H. Cho, "Analog-digital switching mixed mode low ripple high efficiency Li–Ion battery charger," in *Conf. Rec. 36th IEEE IAS Annu. Meeting*, Oct. 2001, pp. 2473–2477.
[2] *BQ2057 Data Sheet*, Texas Instruments Inc., Dallas, TX, 2002.
[3] V. L. Teofilo, L. V. Merritt, and R. P. Hollandsworth, "Advance lithium ion battery charger," *IEEE Aerosp. Electron. Syst. Mag.*, vol. 12, no. 11, pp. 30–36, Nov. 1997.
[4] M. J. Isaacson, R. P. Hollandsworth, P. J. Giampaoli, F. A. Linkowsky, A. Salim, and V. L. Teofilo, "Advance lithium ion battery charger," in *Proc. IEEE 15th Annu. Battery Conf. Appl. Advances*, Jan. 2000, pp. 193–198.

[5] L.-R. Chen, "PLL-based battery charge circuit topology," *IEEE Trans. Ind. Electron.*, vol. 51, no. 6, pp. 1344–1346, Dec. 2004.

[6] *Panasonic Lithium–Ion Coin Data Sheet*, Panasonic Corp., Osaka, Japan, 2003.

[7] C.-C. Tsai, C.-Y. Lin, Y.-S. Hwang, W.-T. Lee, and T.-Y. Lee, "A multi-mode LDO-based Li–Ion battery charger in 0.35μm CMOS technology," in *Proc. IEEE Asia-Pacific Conf. Circuits Syst.*, Dec. 2004, vol. 1, pp. 49–52.

[8] T. Y. Man, P. K. T. Mok, and M. Chan, "A high slew-rate push–pull output amplifier for low-quiescent current low-dropout regulators with transient-response improvement," *IEEE Trans. Circuits Syst. II, Exp. Briefs*, vol. 54, no. 9, pp. 755–759, Sep. 2007.

[9] Product applications of the chip ICE2A0565Z on the web. [Online]. Available: http://www.infineon.com/cms/en/product/channel.html

[10] Y. S. Hwang, C. C. Wang, F. C. Yang, and J. J. Chen, "New compact CMOS Li–Ion battery charger using charge-pump technique for portable applications," *IEEE Trans. Circuits Syst. I, Reg. Papers*, vol. 54, no. 4, pp. 705–712, Apr. 2007.

[11] Y.-L. Ke and Y.-C. Chuang, "A novel high-efficiency battery charger with a buck zero-voltage-switching resonant converter," *IEEE Trans. Energy Convers.*, vol. 22, no. 4, pp. 848–854, Dec. 2007.

[12] H.-J. Chiu, L.-W. Lin, P.-L. Pan, and M.-H. Tseng, "A novel rapid charger for lead-acid batteries with energy recovery," *IEEE Trans. Power Electron.*, vol. 21, no. 3, pp. 640–647, May 2006.

[13] W. Kleebchampee and C. Bunlaksananusorn, "Modeling and control design of a current-mode controlled flyback converter with optocoupler feedback," in *Proc. Int. Conf. Power Electron. Drives Syst.*, 2005, vol. 1, pp. 787–792. no. 16–18.

[14] M. G. Egan, D. L. O'Sullivan, J. G. Hayes, M. J. Willers, and C. P. Henze, "Power-factor-corrected single-stage inductive charger for electric vehicle batteries," *IEEE Trans. Ind. Electron.*, vol. 54, no. 2, pp. 1217–1226, Apr. 2007.

[15] Y.-S. Lee and M.-W. Cheng, "Intelligent control battery equalization for series connected lithium–ion battery strings," *IEEE Trans. Ind. Electron.*, vol. 52, no. 5, pp. 1297–1307, Oct. 2005.

[16] C.-S. Wang, O. H. Stielau, and G. A. Covic, "Design considerations for a contactless electric vehicle battery charger," *IEEE Trans. Ind. Electron.*, vol. 52, no. 5, pp. 1308–1314, Oct. 2005.

[17] M. Chen and G. A. Rincón-Mora, "Accurate, compact, and power-efficient Li–Ion battery charger circuit," *IEEE Trans. Circuits Syst. II, Exp. Briefs*, vol. 53, no. 11, pp. 1180–1184, Nov. 2006.

[18] B. Choi, J. Nho, H. Cha, T. Ahn, and S. Choi, "Design and implementation of low-profile contactless battery charger using planar printed circuit board windings as energy transfer device," *IEEE Trans. Ind. Electron.*, vol. 51, no. 1, pp. 140–147, Feb. 2004.

[19] J. Díaz, J. A. Martín-Ramos, A. M. Pernía, F. Nuño, and F. Fernández Linera, "Intelligent and universal fast charger for Ni–Cd and Ni–MH batteries in portable applications," *IEEE Trans. Ind. Electron.*, vol. 51, no. 4, pp. 857–863, Aug. 2004.

[20] M. A. S. Masoum, S. M. M. Badejani, and E. F. Fuchs, "Microprocessor-controlled new class of optimal battery chargers for photovoltaic applications," *IEEE Trans. Energy Convers.*, vol. 19, no. 3, pp. 599–606, Sep. 2004.

[21] H. Abe, H. Sakamoto, and K. Harada, "A noncontact charger using a resonant converter with parallel capacitor of the secondary coil," *IEEE Trans. Ind. Appl.*, vol. 36, no. 2, pp. 444–451, Mar./Apr. 2000.

[22] Y. Jang and M. M. Jovanovic, "A contactless electrical energy transmission system for portable-telephone battery chargers," in *Conf. Rec. Telecommun. Energy Conf.*, 2000, pp. 726–732.

[23] G. Thiele and E. Bayer, "Current-mode LDO with active dropout optimization," in *Proc. 36th IEEE Power Electron. Spec. Conf.*, 2005, pp. 1203–1208.

Fong-Cheng Yang received the B.S.E.E. degree from the Institute of Electronic Engineering, Fu-Jen Catholic University, Taipei, Taiwan, in 2004. He is currently working toward the Ph.D. degree in the Department of Electronic Engineering, National Taipei University of Technology, Taipei.

His research interest is power management.

Chien-Chih Lai was born in Changhua, Taiwan, in 1980. He received the B.S. degree in electrical engineering from Lung-Hwa University of Science and Technology, Taoyuan, Taiwan, in 2002, and the M.S. degree in engineering science from National Cheng Kung University, Tainan, Taiwan, in 2004. He is currently working toward the Ph.D. degree in the Department of Electronic Engineering and Graduate Institute of Computer and Communication Engineering, National Taipei University of Technology, Taipei, Taiwan.

His research interests include power electronics, electronic system design for portable applications, telecare and mobile-care system design, and wireless sensor networks for medical care applications.

Yuh-Shyan Hwang was born in Taipei, Taiwan, in 1966. He received the B.S.E.E. degree from Feng-Chia University, Taichung, Taiwan, in 1988, and the M.S. and Ph.D. degrees in electrical engineering from National Taiwan University, Taipei, in 1991 and 1996, respectively.

During 1991–1996 and 1996–2003, he was an Instructor and an Associate Professor with the Department of Electrical Engineering, Lee-Ming Institute of Technology and Hwa Hsia Institute of Technology, respectively. Since 2003, he has been with the Department of Electronic Engineering and Graduate Institute of Computer and Communication Engineering, National Taipei University of Technology, Taipei. His current research interests include analog integrated circuits design, mixed-signal integrated circuits design, electronic circuits design, and analog signal processing.

Jiann-Jong Chen was born in Keelong, Taiwan, in 1966. He received the M.S. and Ph.D. degrees in electrical engineering from National Taiwan University, Taipei, Taiwan, in 1992 and 1995, respectively.

From 1994 to 2004, he was with the faculty of Lunghwa University of Science and Technology, Taoyuan, Taiwan. Since August 2004, he has been with the Department of Electronic Engineering, National Taipei University of Technology, Taipei, where he is currently an Associate Professor. His research interests are in the area of mixed-signal integrated circuits and systems for power management.

Ren-Guey Lee (M'07) received the M.S. degree from the Department of Electrical Engineering, National Chen Kung University, Tainan, Taiwan, in 1989, and the Ph.D. degree from the Department of Electrical Engineering, National Taiwan University, Taipei, Taiwan, in 2000.

Since 2002, he has been with the Department of Electronic Engineering and Graduate Institute of Computer and Communication Engineering, National Taipei University of Technology, Taipei, where he is currently a Professor. His research interests include electronic system design for portable applications, medical informatics, telecare and mobile-care system design, and wireless sensor networks for biomedical applications.